Title
Chirality-Induced Magnet-Free Spin Generation in a Semiconductor

Authors
Liu, Tianhan
Adhikari, Yuwaraj
Wang, Hailong
et al.

Publication Date
2024-06-26

DOI
10.1002/adma.202406347

ADVANCED MATERIALS
www.advmat.de

Chirality-Induced Magnet-Free Spin Generation in a Semiconductor

Tianhan Liu, Yuwaraj Adhikari, Hailong Wang, Yiyang Jiang, Zhenqi Hua, Haoyang Liu, Pedro Schlottmann, Hanwei Gao, Paul S. Weiss, Binghai Yan, Jianhua Zhao,* and Peng Xiong**

Electrical generation and transduction of polarized electron spins in semiconductors (SCs) are of central interest in spintronics and quantum information science. While spin generation in SCs is frequently realized via electrical injection from a ferromagnet (FM), there are significant advantages in nonmagnetic pathways of creating spin polarization. One such pathway exploits the interplay of electron spin with chirality in electronic structures or real space. Here, utilizing chirality-induced spin selectivity (CISS), the efficient creation of spin accumulation in *n*-doped GaAs via electric current injection from a normal metal (Au) electrode through a self-assembled monolayer (SAM) of chiral molecules (α-helix L-polyalanine, AHPA-L), is demonstrated. The resulting spin polarization is detected as a Hanle effect in the *n*-GaAs, which is found to obey a distinct universal scaling with temperature and bias current consistent with chirality-induced spin accumulation. The experiment constitutes a definitive observation of CISS in a fully nonmagnetic device structure and demonstration of its ability to generate spin accumulation in a conventional SC. The results thus place key constraints on the physical mechanism of CISS and present a new scheme for magnet-free SC spintronics.

T. Liu, Y. Adhikari, Z. Hua, H. Liu, P. Schlottmann, H. Gao, P. Xiong
Department of Physics
Florida State University
Tallahassee, FL 32306, USA
E-mail: tianhanliu@g.ucla.edu; pxiong@fsu.edu

T. Liu, P. S. Weiss
Department of Chemistry and Biochemistry
University of California, Los Angeles
Los Angeles, CA 90095, USA

H. Wang, J. Zhao
State Key Laboratory of Superlattices and Microstructures
Institute of Semiconductors
Chinese Academy of Sciences
Beijing 100083, China
E-mail: jhzhao@semi.ac.cn

Y. Jiang, B. Yan
Department of Condensed Matter Physics
Weizmann Institute of Science
Rehovot 7610001, Israel

P. S. Weiss
California NanoSystems Institute and Departments of Bioengineering and Materials Science and Engineering
University of California, Los Angeles
Los Angeles, CA 90095, USA

The ORCID identification number(s) for the author(s) of this article can be found under https://doi.org/10.1002/adma.202406347

DOI: 10.1002/adma.202406347

1. Introduction

Controlled generation of spin polarization in semiconductors (SCs) is of broad interest for the underlying physics and spintronics and quantum information science applications. A key ingredient for such applications is efficient electrical spin generation in a nonmagnetic SC and transduction of the resulting spin accumulation/current to electrical signals.[1,2] Charge-spin interconversion is commonly realized by contacting the SC with a ferromagnet (FM), which serves as the spin injection source and a spin detector,[3–5] where the experimental implementation of the spin detection typically takes the forms of a spin-valve or Hanle effect device.[6–8] In the meantime, nonmagnetic pathways for spin generation and detection have attracted increasing interest. These have included the spin Hall effect[9,10] and Edelstein effect[11] for charge-to-spin conversion, and their inverse effects[12] for spin-to-charge conversion. These effects rely on spin-orbit coupling (SOC), and in the case of the Edelstein effect, inversion symmetry breaking (the Rashba effect)[13,14] or topological surface states,[15–17] exploiting helical spin textures in momentum space. In these schemes, the resulting spin polarization is generally orthogonal to the direction of the charge current.

More recently, a new nonmagnetic pathway of charge-to-spin conversion has emerged. The effect, termed chirality-induced spin selectivity (CISS), originates from the interplay of electron orbital motion and structural chirality in real space.[18–22] It manifests as an induced spin polarization in a chiral medium collinear with the charge current along the chiral axis.[19,23,24] The chirality-induced spin polarization was first evidenced in photo-emitted electrons passing through a self-assembled monolayer (SAM) of double-stranded DNA, via direct Mott polarimetry measurements of the photoelectrons in free space.[25] In contrast, in solid-state devices incorporating CISS, the spin detection is usually indirect, for instance, by measuring the spin-valve effect using a FM counter-electrode[26–36] or the circular polarization of electroluminescence from a light-emitting diode containing a chiral hybrid perovskite hole injector.[37] In the latter, the optical detection rids of the need for a magnetic spin detector. Despite the extensive research and preponderance of experimental

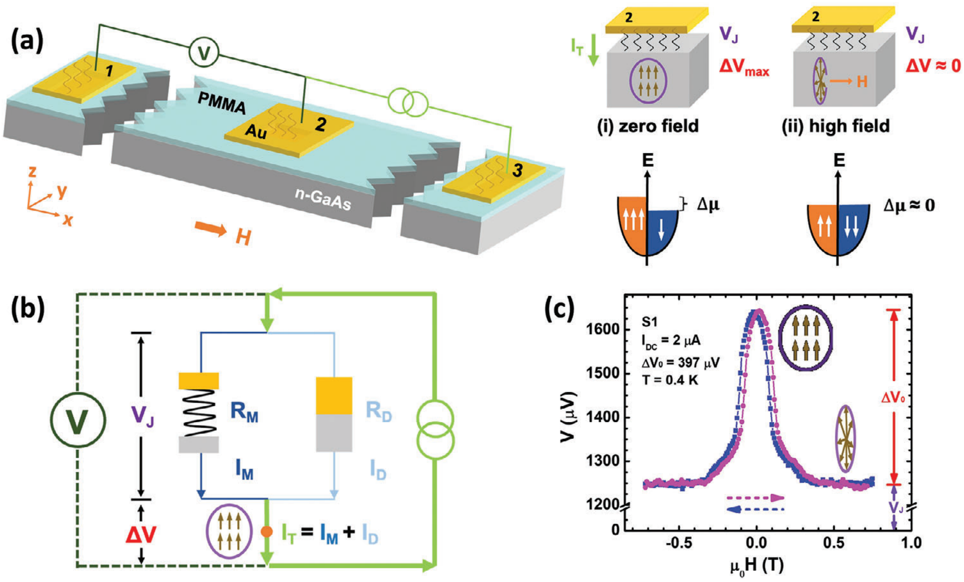

Figure 1. Device schematics and representative Hanle curve. a) Schematics of the *n*-GaAs/AHPA-L/Au junctions and the measurement setup. A current is applied between contacts 3 to 2, and voltage is measured between contacts 2 and 1. Here, the total voltage measured, V, is the sum of junction voltage (V_J) and the spin accumulation voltage (ΔV). The diagrams on the right depict two different spin states in a chiral molecular junction under electrical current injection: (i) At zero field, the spin polarized current produces spin accumulation in GaAs under contact 2, resulting in spin-splitting of the chemical potential ($\Delta\mu$) and additional voltage (ΔV). (ii) When an in-plane magnetic field is applied, the accumulated spins precess around the field and become fully dephased at sufficiently high field, consequently ΔV decreases to zero while V_J remains essentially unchanged. b) An equiv. circuit diagram of the molecular junction. R_M (I_M) and R_D (I_D) are the resistances of (currents through) the molecular and direct contact in the molecular junction, respectively. I_T is the total current through the junction. c) A representative Hanle curve $V(B)$: The measured total voltage V versus in-plane magnetic field, as the sum of V_J and ΔV. The blue and magenta dashed arrows indicate the sweep direction of the magnetic field. ΔV_0 is the value of ΔV at zero field.

results, even in the simplest device structures of two-terminal spin-valves, the interpretation of the experiments is fraught with controversy.[21,22] The open questions include spin versus orbital polarization,[20,38] the origin of the SOC necessary for producing spin polarization,[19,21,35] and the possible relevance of spinterface effects,[39] in order to account for the extraordinarily large magnetoresistance (MR) observed in many experiments.[19,21,33,36] In fact, the very existence of MR in the two-terminal spin valves has been questioned because of its apparent conflict with the Onsager relation.[40–43] Answers to these questions thus have direct implications for the understanding of the physical mechanism of the CISS effect, which remains elusive.[21,22] Therefore, for definitive elucidation of both the physical origin and device manifestations of CISS, direct measurements of the polarized spins in robust solid-state/chiral-molecule hybrid devices are imperative.[44]

Here, we present direct experimental evidence for CISS-induced spin accumulation in a conventional nonmagnetic SC. The spin accumulation is created in a Si-doped GaAs via charge current injection from a Au electrode through an α-helix L-polyalanine (AHPA-L) SAM, and detected via measurement of the Hanle effect without using a magnetic electrode. The Hanle effect data obtained from different devices and the full bias current-temperature parameter space are shown to collapse onto a single scaling function. Notably, the Hanle signals in the *n*-GaAs/AHPA-L/Au junctions follow a distinct power-law temperature (T) dependence and a nonmonotonic log-normal-like dependence on the bias current. The bias dependence qualitatively resembles that in conventional FM/SC devices,[45–47] while the power-law T-dependence with varying onset temperatures may reflect the combination of CISS spin injection via the chiral molecules and spin relaxation in the SC. The experiments thus present an unambiguous case for structural chirality-induced magnet-free electrical spin generation and detection in a SC. The observation of CISS effect in the devices free of any magnetic element places several specific constraints on its theoretical description and suggests a new scheme for magnet-free SC spintronics.

2. Results

2.1. Spin Accumulation Measurement

A schematic diagram depicting the molecular junction device structure and setup for the Hanle measurements is shown in **Figure 1a**. The epitaxial layer of Si-doped GaAs was grown by molecular beam epitaxy (MBE) on a semi-insulating GaAs(001) substrate. The carrier (electron) density was determined to be 7.1×10^{18} cm^{-3} at 5 K and below from Hall measurements (details in SI 1, Supporting Information). The device fabrication process, including the formation and preservation of the AHPA-L SAM, is essentially the same as that employed for making the molecular spin-valve devices based on (Ga,Mn)As.[32,35] The AHPA-L molecule used is based on α-helix L-polyalanine (H-CAAAA KAAAA KAAAA KAAAA KAAAA KAAAA KAAAA K-OH), where C, A, and K represent cysteine, alanine, and lysine, respectively. α-helix has a right-hand-spiral conformation and the length of AHPA-L molecule used is 5.4 nm. The cysteine in the N-terminus contains thiol that facilitates SAM formation on GaAs. The packing density in the SAM is presumed to be similar to that on Au(111) (≈1 molecule/nm^2).[48] We recently demonstrated that the (Ga,Mn)As/AHPA-L/Au molecular junctions consistently yield pronounced spin-valve magnetoconductance,[32,35] indicating that the SC-based chiral molecular junctions are a robust and reliable platform for measuring spin-selective transport through chiral molecular SAMs. Most notably, the use of a SC substrate effectively mitigates electrical shorting through defects in the molecular SAM, which is typically fatal in all-metal molecular junctions. Therefore, we expect that replacing the (Ga,Mn)As with a heavily *n*-doped GaAs will produce a molecular junction of similar characteristics, which enables spin detection via the Hanle effect without a magnetic spin analyzer.

The Hanle measurements were performed in a three-terminal (3T) configuration by applying an in-plane magnetic field (Figure 1a). A fabricated device typically consists of multiple junctions (3 to 4) of size 5×5 µm^2 with two large reference electrodes. The experimental details for the device fabrication, including the molecular assembly and electrical measurements, are described in the Experimental Section. Here, the expectation is that a charge current injected into or extracted from the *n*-GaAs will result in spin accumulation of perpendicular polarization due to the CISS effect in the AHPA-L. The spin accumulation, in the form of a spin splitting of the chemical potential, $\Delta\mu = \mu_\uparrow - \mu_\downarrow$, is detected as an additional voltage (ΔV) between the Au and *n*-GaAs electrodes in series with the normal voltage drop due to carrier transport across the junction (V_J). Upon application of an increasing in-plane magnetic field, the spin accumulation (ΔV) is diminished due to the resulting precession and dephasing of the perpendicularly polarized spins, reducing the signal to the baseline voltage of V_J at sufficiently high field. Because of the nonlinear response of ΔV to the bias current, we plot the results as $V(B)$ instead of MR.

Figure 1b shows an equivalent circuit diagram of the chiral molecular junction and a schematic illustration of the expected experimental outcome from the picture of chirality-induced spin injection and accumulation. First, we note that the SAMs in the junctions are most likely not perfect[49–51]; defects are almost always present in SAMs at such device scales (µm).[52] As a result, electron transport through the junctions comprises two parallel contributions to the total charge current (I_T): one through the chiral molecules, I_M, and the other through the pinholes in the SAM (direct contact between the Au and *n*-GaAs), I_D. The scenario is similar to that in (Ga,Mn)As spin-valve devices.[32,35] Here, I_M is spin polarized and induces spin accumulation in the GaAs, while I_D does not. The total voltage measured then consists of two components: $V = V_J + \Delta V$, where V_J is the voltage drop across the junction and ΔV is the spin accumulation voltage in the GaAs (due to $\Delta\mu$). Upon application of an in-plane magnetic field, the magnitude of ΔV is expected to decrease with increasing field and reach zero, concurrently the measured voltage V becomes constant if V_J has negligible dependence on the applied magnetic field.

Figure 1c shows a representative measurement of the total voltage as a function of the applied in-plane magnetic field for a *n*-GaAs/AHPA-L/Au junction. The resulting $V(B)$ curve is qualitatively consistent with the expectations described above: The measured voltage is maximum at zero field and decreases with increasing B, reaching a constant value at ≈300 mT. The $V(B)$ curve is not exactly Lorentzian and shows small hysteresis in the field sweeps; both features are discussed later.

Figure 2a shows the I-V curves for the same junction measured at 0.4 K in zero and 600 mT in-plane field, and the result is in full agreement with the $V(B)$ data: At 600 mT, above the saturation field in $V(B)$, the I-V is linear, indicating an Ohmic junction resistance that has negligible dependence on the applied field. At zero field, the I-V shows "nonlinear" behavior in the low-bias regime. However, there is compelling evidence that the apparent "nonlinearity" is not intrinsic MR of the junction, but rather an additional voltage due to spin accumulation in series with the Ohmic junction: i) A moderate magnetic field of 300 mT eliminates the "nonlinearity" and restores the linear I-V for the junction. ii) With increasing bias current, the zero-field I-V approaches that in the 600-mT field and becomes linear. From the two I-V curves in Figure 2a, we can extract the amplitudes of the Hanle signals, i.e., the magnitudes of the additional voltage in zero field, ΔV_0, at different bias currents, as illustrated in the inset of Figure 2a. The same Hanle amplitudes can also be determined from DC and low-frequency AC measurements of $V(B)$ at different fixed bias currents. A set of such measurements on the same junction with different AC currents is shown in Figure 2b. The resulting Hanle amplitudes are plotted in Figure 2c; the different measurements produce essentially identical results. ΔV_0 shows a nonmonotonic dependence on the bias current; it initially increases sharply with increasing current and then decreases precipitously and vanishes at higher currents. Another notable feature in Figure 2a,c is that ΔV_0 is exactly antisymmetric upon reversal of the bias current, which is corroborated by the fact that the DC and AC measurements produce the same results.

We have fabricated and evaluated ≈20 such devices, each having 3–4 junctions. Six devices yielded 11 chiral molecular junctions exhibiting signals qualitatively similar to those shown in Figure 2 out of 39 junctions measured. The majority of the results shown here are from four junctions from four different samples, on which full sets of temperature- and bias-dependent measurements were performed. Importantly, there were distinct and easily identifiable "failure mode" for the chiral molecular junction devices that did not show Hanle signal (details in SI 3, Supporting Information). Similar measurements were also performed for control samples without any chiral molecules. Neither the I-V nor the $V(B)$ showed any discernible magnetic field dependence (details in SI 4, Supporting Information). The control experiments provide direct evidence supporting the conjecture that the current through the defects in the chiral SAM (I_D) does not contribute to the spin accumulation (Figure 1b).

2.2. Universal Temperature and Bias Current Dependences

We now examine the general behavior of the Hanle amplitude, ΔV_0, in the temperature-bias current space. **Figure 3a** shows the

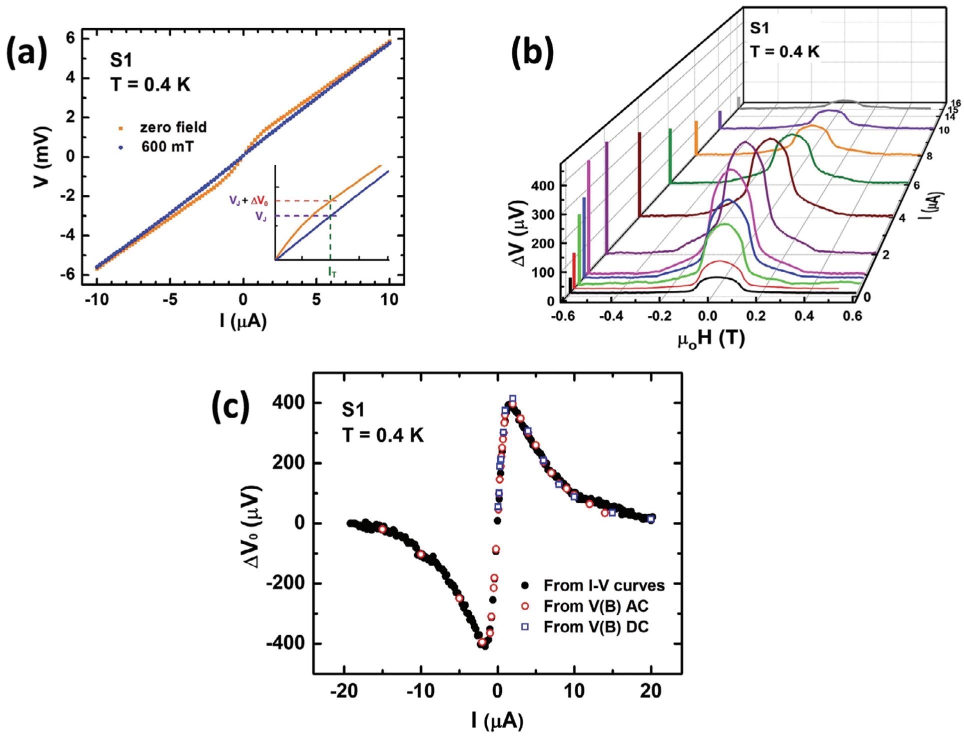

Figure 2. I-V characteristics and bias-dependent Hanle signals. a) I-V characteristics of the *n*-GaAs/AHPA-L/Au junction in zero (orange) and in-plane magnetic field of 600 mT (blue). The inset shows a close-up of the I-V curves, which depicts how ΔV_0 at a fixed current is extracted from the I-V. b) Spin accumulation voltage versus applied field measured at different AC bias currents at 0.4 K. c) The Hanle amplitude, ΔV_0, defined as the spin accumulation voltage at zero field, extracted from I-V curves in (a), AC $V(B)$ curves in (b), and DC $V(B)$ measurements (Figure S2, Supporting Information), as a function of bias current.

$\Delta V(B)$ curves for the junction in Figure 1 taken at various temperatures with a bias current of 2 μA. Evidently, ΔV_0 decreases with increasing temperature and vanishes at ≈6.3 K in S1. Similar measurements were carried out for varying bias currents on both sides of the peak of the $\Delta V_0(I)$ (Figure 2c); the resulting $\Delta V_0(T)$ for different bias currents are plotted in Figure 3b. Interestingly, ΔV_0 follows the same T-dependence for all bias currents with the same onset temperature T_0, as shown by the collapse of all the $\Delta V_0(T)$ data in Figure 3b onto a single curve by scaling of $\Delta V_0(T)$ for different currents with their respective 0.4 K values, $\Delta V_0(0.4\ K)$, as shown in Figure 3c. All the scaled data are well described by:

$$\frac{\Delta V_0\,(T)}{\Delta V_0\,(0.4K)} = 1 - \left(T/T_0\right)^{5/2} \tag{1}$$

Moreover, the $\Delta V_0(T)$ for different samples can also be scaled to a single function of the reduced temperature, T/T_0. Figure 3d shows $\Delta V_0(T)$ for three different samples measured at their respective current of peak ΔV_0 value, I_p. The magnitudes of ΔV_{0p} for the three junctions differ greatly, 398 μV, 144 μV, and 11 μV for S1, S4, and S2 respectively. Curiously, the onset temperatures of the Hanle signals for the junctions exhibit similarly large variations, which appear to correlate with their magnitude, at 6.3 K, 2.3 K, and 1.2 K, respectively. Despite the large variations of ΔV_0 and T_0, the normalized $\Delta V_0(T)$ for the three junctions show the same dependence on the reduced temperature T/T_0, as shown in Figure 3e. Here the data for different samples in Figure 3d are scaled with their respective zero-temperature values and onset temperatures. The $\Delta V_0(0K)$ and T_0 values are obtained by fitting each curve in Figure 3d to **Equation 1**. Scaling with $\Delta V_0(0K)$, instead of $\Delta V_0(0.4\ K)$, is necessary for S4 and S2 because of their relatively low T_0.

The bias current dependences of the Hanle signals at different temperatures and in different samples show similar universality. **Figure 4a** shows the variation of ΔV_0 with bias current for junction S1 at different temperatures. With increasing temperature, ΔV_0 decreases over the entire bias range, in such a way that the bias dependence remains unchanged; most notably, the peak current I_p stays essentially constant with changing temperature. Figure 4b shows the data in Figure 4a normalized by their respective peak values of ΔV_0, ΔV_{0p}. The data at all temperatures collapse onto a single curve, indicating a common bias-dependence that is independent of temperature. Moreover, for different samples, while the peak values of ΔV_0 and the peak currents vary greatly (Figure 4c), all the $\Delta V_0(I)$ data once again fall onto a single curve when ΔV_0 and bias current are normalized by their respective peak values; the scaling behavior is evident in Figure 4d.

The consistency of the experimental results across the different junctions and a common underlying temperature-bias current dependence have a striking manifestation, shown in Figure S5 (Supporting Information): The scaled results show that the signal at 0.4 K in junction S2 closely resembles the

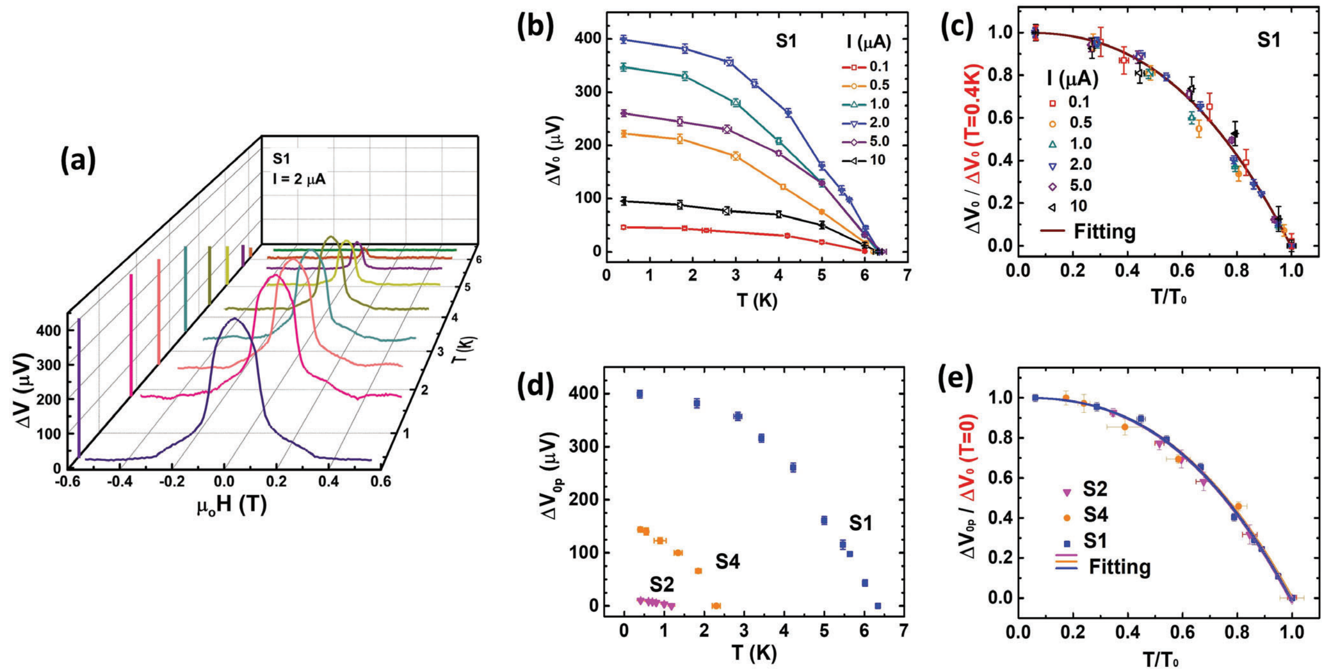

Figure 3. Universal temperature dependence of the Hanle amplitude. a) $\Delta V(B)$ for S1 at different temperatures measured at a fixed AC bias current of 2 μA. b) Temperature dependence of the Hanle amplitude, ΔV_0, at different AC bias currents. c) Scaling of the $\Delta V_0(T)$ data for different bias currents in (b) with its values at 0.4 K and the onset temperature T_0. The solid line is a fit to Equation (1). d) Temperature dependence of the peak Hanle amplitude, ΔV_{0p}, for three different samples. e) Scaling of the curves in (d) with their respective zero-temperature values and onset temperatures. The $\Delta V_0(0K)$ and T_0 values are obtained by fitting each curve in (d) to Equation (1). The solid lines are the fittings to Equation (1) with scaling.

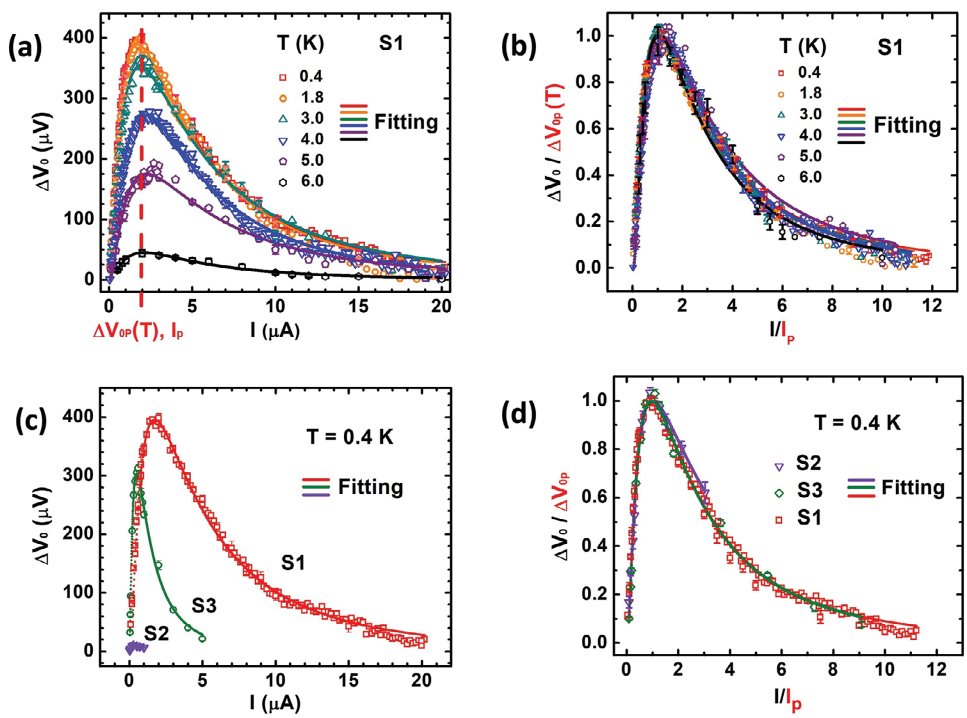

Figure 4. Universal bias current dependence of the Hanle amplitude. a) Bias current dependence of ΔV_0 at different temperatures for S1. The magnitude of ΔV_0 first increases then decreases with the bias current. The peak value of ΔV_0 is defined as ΔV_{0p} at the current of I_p. b) Scaling of the $\Delta V_0(I)$ data in (a) for different temperatures with their respective values of ΔV_{0p} and I_p. c) Bias current dependence of ΔV_0 for three different samples at 0.4 K. d) Scaling of the data in (c) with their respective values of ΔV_{0p} and I_p. The solid lines in all panels are best fits to Equation (4).

signal at 5.4 K for junction S1 (details in SI 5, Supporting Information).

3. Discussion

3.1. 3T Hanle Measurement

The Hanle effect has been one of the most widely utilized and effective methods of measuring spin lifetime, spin accumulation, and spin transport in SCs. The measurements have been implemented in both nonlocal four-terminal (NL-4T)[7,8] and simplified 3T geometries.[4,53] A notable controversy in the field concerns the reliability of 3T Hanle measurements for spin detection.[53] Specifically, in devices with oxide barriers, it was shown that i) the amplitudes of the 3T Hanle signals often greatly exceeded the values expected from the Valet-Fert theory[54,55] and NL-4T measurements[56,57] and, ii) the spin lifetimes determined from the 3T Hanle curves were consistently 1–3 orders of magnitude smaller than theoretical predictions[58] and results of electron spin resonance[59] and NL-4T measurements.[53] This has led to critical questions and conclusions that the 3T Hanle measurement does not probe spin injection and accumulation. However, it is important to note that there is no fundamental physical reason prohibiting spin injection and detection in the 3T Hanle setup. Moreover, a ubiquitous component of the 3T Hanle devices showing the anomalous properties is an artificial oxide tunnel barrier, which hosts the localized electronic states necessary in the alternative models proposed to account for the anomalous observations.[54,60] In contrast, in all-epitaxial heterostructure devices free of oxide barriers, the 3T Hanle results do not show the anomalous behaviors described above.[46,61,62] In particular, we recently performed direct comparative measurements of 3T and NL-4T effects in the same devices of epitaxial $Fe/Al_{0.3}Ga_{0.7}As$ heterostructures; the 3T Hanle signals exhibit broad similarities with the NL-4T results in all aspects, including similar spin lifetimes and consistent Hanle amplitudes.[46] The experiments provided compelling evidence that in devices engineered to minimize localized states in spin injectors and detectors, the 3T Hanle effect reliably probes spin accumulation and its dynamics in the SC channel.

For the molecular junction devices studied in this work, a direct comparative NL-4T Hanle measurement is exceedingly difficult to implement because a lithographical step would be required after the molecular assembly, which would destroy the AHPA-L SAM. Nevertheless, many aspects of the 3T Hanle data, including the field-suppression of the I-V nonlinearity discussed above and the resulting physical parameters (e.g., spin lifetime) presented below, point to spin accumulation in the *n*-GaAs as the physical origin of the 3T Hanle effect. Furthermore, because the molecular junctions are free of any magnetic materials, the spinterface effect[39] can be ruled out as the origin of the field-dependent signals here.

3.2. Spin Accumulation Measurement

The results in Figures 3c,e and 4b,d indicate that the amplitude of the Hanle signal varies independently with temperature and bias current. Analytically, the Hanle amplitude ΔV_0 at temperature T and bias current I for any sample can be described by the same expression:

$$\Delta V_0 \;(T, I) = \;\Delta V_{max} f\;(T)\, g\,(I) \tag{2}$$

where,

$$f\;(T) = \;1 - \beta\left(T/T_0\right)^{\alpha} \tag{3}$$

and

$$g\;(I) = \;exp\left(-\frac{\left[\ln\left(I/I_p\right)\right]^2}{w}\right) \tag{4}$$

Several features are worth noting: i) T_0 is independent of I; ii) I_p is independent of T; iii) $\Delta\, V_{max} = \;\Delta V_0(0,I_p)$, T_0, and I_p are sample-specific and determined directly from experiment; iv) both T_0 and I_p show positive correlation with ΔV_{max}. The best fits of the data in Figure 3c,e to **Equation 3** yield β of unity (1±0.02) and α of 5/2 (details in SI 6, Supporting Information). The temperature dependence in Equation 3 resembles that of the magnetization of an isotropic FM described by the Bloch's law,[63] but with a power law exponent of 5/2 instead of 3/2. A rendition of $\Delta V_0(T,I)$ in the full temperature-bias current space for S1 is shown as a false-color plot derived from **Equation 2** in Figure S8 (Supporting Information).

The striking nonmonotonic bias current dependence of the Hanle signals can be quantitatively described by the log-normal-like function of Equation 4. The unscaled data in Figure 4a,c are fit to Equation 2, and the best fits are shown as the solid lines. Here w is practically the only adjustable fitting parameter, as ΔV_{max} and I_p are obtained directly from the experimental data with high accuracy. Interestingly, the resulting w from the three different samples in Figure 4c are essentially the same (2.26 ± 0.04), despite the large differences in the Hanle amplitude and peak current. The w derived from junction S1 at different temperatures (Figure 4a) shows a slight, but noticeable, decrease with increasing temperature near T_0. More details of the fitting procedures are given in SI 6 (Supporting Information). The values of the physical and fitting parameters for the same sample at varying temperature and for different samples at the same temperature are listed in Tables S2 and S3 (Supporting Information), respectively (details in SI 8, Supporting Information).

We now turn to the physical implications of the results outlined above. First, we summarize the key observations from the Hanle measurements: i) The Hanle amplitude follows a non-monotonic log-normal-like dependence on the bias current for all samples. ii) The Hanle amplitude exhibits a well-defined power-law decrease with increasing temperature at all bias currents for all samples. iii) The onset temperature (T_0) of the Hanle signal is sample dependent, and correlates positively with its maximum amplitude.

For the bias dependence, we first note the spurious nature of the peak current value, I_p, due to the presence of parallel conduction current through the direct contact. Therefore, any correlation of I_p with ΔV_{max} must be viewed with caution. Nevertheless, we emphasize that the parallel conduction current has no bearing on the bias-dependence, because of the intrinsic linear I-V characteristics of the junctions; both I and I_p through the molecular SAM differ from their respective total values through the junction by the same constant scaling factor, thus not affecting I/I_p.

Note that the close similarities of the bias dependence of the Hanle signals here and that of the spin accumulation in conventional FM/SC devices.[45–47,64] Most relevant are the cases of 2T and 3T FM/SC devices, in which the bias dependences of local spin accumulation have been measured both electrically[46,47] and optically.[45,64] Electrically, the spin accumulation was measured via spin-valves[47] and the Hanle effect[46]; in both cases, the magnitudes of the spin accumulation were observed to exhibit similar nonmonotonic bias dependences. The nonmonotonic behavior of the spin accumulation was attributed to a combination of linear increases with injection current and exponential decreases of the spin polarization, which was demonstrated explicitly by Fujita et al.[47] Optically, the spin accumulation was determined from the circular polarization of the electroluminescence in FM/SC spin LEDs.[64] Notably, from the electroluminescence of the current injection from Fe into n-GaAs, Hickey et al.[45] identified a bias-dependent polarization at low temperature that resembles our observations in the chiral molecular junctions (Figure 4). In all cases, the steep drop-off at high biases was attributed to enhanced Dyakonov-Perel (DP) spin relaxation with increasing kinetic energy (momentum) of the injected electrons, for the DP process is the dominant spin relaxation mechanism at high doping densities.[65]

Evident from the universality of the bias dependence in Figure 4 is that the value of w is essentially the same for all samples despite the large differences of the peak Hanle amplitude. The constancy of w is strongly suggestive that the bias dependence reflects the spin dynamics in the n-GaAs and is likely independent of the details of the molecular junctions. In this respect, our previous study of the Hanle effect in epitaxial Fe/n-AlGaAs devices provided a useful reference.[46,47] The detailed comparison of molecular junction n-GaAs/AHPA-L/Au with epitaxial Fe/n-AlGaAs is presented in SI 9 (Supporting Information). As shown in Figure S10c (Supporting Information), the value of w decreases continuously with the carrier density of the n-AlGaAs and smoothly approaches the value 2.3±0.1 in the n-GaAs in this work. This consistent carrier density dependence of w further attests to the common underlying physical processes in our magnet-free chiral molecular junctions and conventional FM/SC devices.

In contrast, the distinct temperature dependence of the Hanle signals observed in our chiral molecular junction devices cannot be understood based solely on spin relaxation in n-GaAs. The magnitude of spin accumulation in a normal conductor under spin injection is approximated well by the simplified Valet-Fert equation: $\Delta V/j = \gamma^2 r_N$,[66] where j is the injection current density, γ is the spin injection/detection efficiency, and r_N is the spin-resistance of the normal conductor (details in SI 10, Supporting Information). In our case, the normal conductor is degenerately doped n-GaAs, in which the temperature dependence of r_N originates from that of the spin lifetime, $r_N \sim \sqrt{\tau_s}$ (details in SI 11, Supporting Information). Theoretically, different power-law T-dependences were predicted based on the different spin relaxation mechanisms,[2,67] including T^{-5} from the Elliot-Yafet process.[68] However, such spin relaxation depends primarily on spin-lattice interactions, which are expected to saturate at low temperatures; more importantly, $\sqrt{\tau_s}$ would yield a direct power-law decrease of spin accumulation with increasing temperature, instead of that of Equation (3). Experimentally, in conventional FM/SC structures, the spin accumulation signals in n-GaAs were observed to exhibit rather weak temperature dependences, persisting above 100 K.[6] This result is in contrast to the steep power-law decrease and low onset temperatures observed in the chiral molecular junctions in this work. Most notably, as is evident in Figure 3c, the Hanle signal vanishes at rather low temperatures, and the onset temperatures of different junctions show distinct correlation with their peak amplitudes. These features suggest that the observed T-dependence predominantly originates from that of γ. We note that in conventional magnetic tunnel junctions, a similar power-law decrease (with an exponent of 3/2) of the magnetoconductance (ΔG) was observed.[69] The T-dependence there was ascribed to the variation of spin polarization due to thermally excited spin waves. More interestingly, despite the common T-dependence in different devices, it was observed that both the amplitude of spin polarization (the equiv. of ΔV_{max} in this work) and the critical temperature (the equiv. of T_0) were sensitive to the interface quality,[69] which are similar to the behaviors of our junctions, shown in Figure 3d. The well-defined T-dependence in our chiral molecular junctions thus likely reflects that of the mechanism of spin selectivity, whose understanding should provide important new insight into the physical origin of CISS.

Another intriguing feature of our results is the remarkably small bias currents for producing the sizable spin accumulation and for inducing spin relaxation ($I > I_p$). For comparison, these current densities are ca. two orders of magnitude smaller than those in similar conventional SC/FM devices.[6,46] This result is in spite of the likely presence of parallel conduction in the junctions. The anomalously small current densities are also reflected in the unphysical values of γ inferred from the Valet-Fert model.[66] For instance, based on the low-current ($I < I_p$) data in Figure 2c, the Valet-Fert model yields $\gamma \sim 10$ (details in SI 10, Supporting Information). We surmise that this result reflects the discrete nature of the electron transport through individual chiral molecules; namely, the effective current density is much greater than the average value obtained using the entire junction area, supporting the proposition that CISS is a single-molecule effect rather than a collective effect.[70,71]

Finally, we examine the line-shape of the Hanle signals. The electrical Hanle effect, which can involve spin precession, spin relaxation, and spin drift/diffusion, provides rigorous elucidation of spin dynamics via analysis using the spin drift-diffusion equation.[62,65,67] In the absence of spin drift or diffusion or both, the Hanle curve is approximated well by a Lorentzian function,[4,7] whose full width at half maximum (FWHM) provides a convenient measure to determine the spin lifetime. In our devices, the spin lifetimes estimated from the widths of the Hanle curves range from 100 to 300 ps (details are in SI 12, Supporting Information), which is in general agreement with the values expected in GaAs at such carrier densities.[65] The line-shapes of the Hanle signals in the chiral molecular junctions are not precisely Lorentzian. Various factors may contribute to the deviation of the Hanle signal from a pure Lorentzian.[4,67] First, we note that the Hanle amplitudes are not affected by the line-shapes;

thus, the deviations from the Lorentzian have no impact on the analyses of the bias and temperature dependences of the Hanle effect. Moreover, in our devices, most of the Hanle curves appear to be superpositions of two Lorentzian-like curves. In some cases, the central peak is sharp (e.g., Figure S12 in SI 13, Supporting Information), resembling that observed in conventional Fe/n-GaAs devices due to the dynamic nuclear polarization (DNP) effect.[62] Moreover, the long nuclear spin lifetime could cause a retardation in the field response, resulting in the apparent hysteresis in the Hanle curves. Contribution from DNP may be rigorously ascertained by examining the field orientation dependence of the Hanle signal.[62] Confirmation of the dynamic polarization of the long-lived nuclear spins in the SC via CISS in the chiral molecular junctions would open a new pathway for fundamental studies of CISS and provide a platform for integral quantum information storage.[22,72]

4. Conclusions

Utilizing the robust device platform of SC-based chiral molecular junctions, we demonstrated CISS-induced spin accumulation in a conventional SC and its direct detection via the Hanle effect. The Hanle effect follows distinct universal temperature and bias current dependences. We anticipate using well-defined, quantitative experimental results to elucidate the physical mechanism of CISS. Practically, the successful incorporation of CISS into a fully nonmagnetic device architecture presents a new scheme of magnet-free SC spintronics.

5. Experimental Section

Materials: The AHPA-L in the experiments was obtained from GenScript, LLC. The resistivity of the commercial semi-insulating GaAs (001) is larger than $1 \times 10^7\ \Omega \cdot cm$. Molecules were dissolved in pure ethanol at 1 mM concentration. The AHPA-L solution was kept at -18 °C for storage.

The Si-doped GaAs substrates were grown by MBE. A 100 nm-thick GaAs buffer layer was first grown on semi-insulating GaAs (001) at 560 °C. A 400 nm-thick GaAs layer doped with Si was later grown at the same temperature. The results shown in this paper are from two GaAs substrates with carrier concentrations of $5.0 \times 10^{18}\ cm^{-3}$ and $7.2 \times 10^{18}\ cm^{-3}$.

Device Fabrication Process: The Hanle devices were fabricated in three steps: junctions were defined by electron-beam lithography (EBL); the oxide layer on GaAs was removed and AHPA-L was assembled on the junctions; and the top Au electrodes were deposited. The parameters are similar to the fabrication procedure of CISS spin-valve devices previously reported.[32,35]

The junction size is $5 \times 5\ \mu m^2$ in all devices. The top electrode consists of 5 nm of Cr and 35 to 40 nm of Au. During the evaporation, the sample was mounted on an angled stage of 15° to ensure the coverage and continuity of the metal film at the edge of the junctions. The substrate temperature was maintained between −30 °C and −50 °C via liquid nitrogen cooling. For both the spin-valve devices studied previously[32,35] and the Hanle devices studied in this work, junctions were also fabricated without the Cr adhesion layer and measured. The two types of devices yielded essentially the same results, whereas the junctions with Cr adhesion layers tended to be mechanically more robust.

To obtain the carrier density of the GaAs substrate, Hall bar devices were patterned by photolithography followed by wet chemical etching. The GaAs etchant was H_2SO_4:H_2O_2:H_2O (1:8:40) and the etching rate was 12.6 nm s^{-1}. Most devices were etched to a depth of 430—450 nm.

Electrical Measurements: In Hanle measurements, samples were fixed on a socket with a copper base and wired by hand with silver paint and Pt wire. In the Hall measurements, contacts were made via indium soldering to reduce the contact resistance. All samples were measured in an Oxford ^{3}He cryostat. DC measurements were done with Keithley 2400 as the current source and HP 3458 as the voltmeter. AC measurements were performed with SR2124 dual-phase analog lock-in amplifiers.

In all Hanle measurements presented in this manuscript, the magnetic field was applied parallel to the sample surface.

Supporting Information

Supporting Information is available from the Wiley Online Library or from the author.

Acknowledgements

T.L., Y.A., and H.W. contributed equally to this work. The authors acknowledge helpful discussions with Profs. Louis Bouchard, Vladimiro Mujica, Stephan von Molnár, and Julio L. Palma Anda. The work at FSU is supported by NSF grants DMR-1905843, DMR-2110814 and DMR-2325147. The work at UCLA is supported by NSF grant CHE-2004238 and the W. M. Keck Foundation through the Keck Center on Quantum Biology. The work at IOS is supported by the MOST grant 2021YFA1202200, the CAS Project for Young Scientists in Basic Research (YSBR-030), and the Strategic Priority Research Program of the Chinese Academy of Sciences under Grant No. XDB44000000. The work at Weizmann Institute of Science is supported by European Research Council (ERC Consolidator Grant "Non-linearTopo", No. 815869).

Conflict of Interest

The authors declare no conflict of interest.

Data Availability Statement

The data that support the findings of this study are available from the corresponding author upon reasonable request.

Keywords

chirality-induced spin selectivity, Hanle effect, molecular junctions, molecular spintronics, spin transport

Received: May 3, 2024
Revised: June 9, 2024
Published online:

[1] S. A. Wolf, D. D. Awschalom, R. A. Buhrman, J. M. Daughton, S. von Molnár, M. L. Roukes, A. Y. Chtchelkanova, D. M. Treger, *Science* **2001**, *294*, 1488.
[2] I. Žutić, J. Fabian, S. Das Sarma, *Rev. Mod. Phys.* **2004**, *76*, 323.
[3] G. Schmidt, D. Ferrand, L. W. Molenkamp, A. T. Filip, B. J. van Wees, *Phys. Rev. B* **2000**, *62*, R4790.
[4] S. P. Dash, S. Sharma, R. S. Patel, M. P. de Jong, R. Jansen, *Nature* **2009**, *462*, 491.
[5] M. Ciorga, A. Einwanger, U. Wurstbauer, D. Schuh, W. Wegscheider, D. Weiss, *Phys. Rev. B* **2009**, *79*, 165321.
[6] X. Lou, C. Adelmann, M. Furis, S. A. Crooker, C. J. Palmstrøm, P. A. Crowell, *Phys. Rev. Lett.* **2006**, *96*, 176603.

[7] X. Lou, C. Adelmann, S. A. Crooker, E. S. Garlid, J. Zhang, K. S. M. Reddy, S. D. Flexner, C. J. Palmstrøm, P. A. Crowell, *Nature Phys.* **2007**, *3*, 197.
[8] O. M. J. van 't Erve, A. T. Hanbicki, M. Holub, C. H. Li, C. Awo-Affouda, P. E. Thompson, B. T. Jonker, *Appl. Phys. Lett.* **2007**, *91*, 212109.
[9] Y. K. Kato, R. C. Myers, A. C. Gossard, D. D. Awschalom, *Science* **2004**, *306*, 1910.
[10] J. Wunderlich, B. Kaestner, J. Sinova, T. Jungwirth, *Phys. Rev. Lett.* **2005**, *94*, 047204.
[11] V. M. Edelstein, *Solid State Commun.* **1990**, *73*, 233.
[12] A. Soumyanarayanan, N. Reyren, A. Fert, C. Panagopoulos, *Nature* **2016**, *539*, 509.
[13] E. I. Rashba, *Soviet Phys. Solid State* **1960**, *2*, 1109.
[14] A. Manchon, H. C. Koo, J. Nitta, S. M. Frolov, R. A. Duine, *Nature Mater.* **2015**, *14*, 871.
[15] J. E. Moore, *Nature* **2010**, *464*, 194.
[16] C. H. Li, O. M. J. van 't Erve, J. T. Robinson, Y. Liu, L. Li, B. T. Jonker, *Nat. Nanotechnol.* **2014**, *9*, 218.
[17] B. Yan, C. Felser, *Annu. Rev. Cond. Mater. Phys.* **2017**, *8*, 337.
[18] R. Naaman, D. H. Waldeck, *J. Phys. Chem. Lett.* **2012**, *3*, 2178.
[19] R. Naaman, D. H. Waldeck, *Annu. Rev. Phys. Chem.* **2015**, *66*, 263.
[20] Y. Liu, J. Xiao, J. Koo, B. Yan, *Nat. Mater.* **2021**, *20*, 638.
[21] F. Evers, A. Aharony, N. Bar-Gill, O. Entin-Wohlman, P. Hedegård, O. Hod, P. Jelinek, G. Kamieniarz, M. Lemeshko, K. Michaeli, V. Mujica, R. Naaman, Y. Paltiel, S. Refaely-Abramson, O. Tal, J. Thijssen, M. Thoss, J. M. van Ruitenbeek, L. Venkataraman, D. H. Waldeck, B. Yan, L. Kronik, *Adv. Mater.* **2022**, *34*, 2106629.
[22] C. D. Aiello, J. M. Abendroth, M. Abbas, A. Afanasev, S. Agarwal, A. S. Banerjee, D. N. Beratan, J. N. Belling, B. Berche, A. Botana, J. R. Caram, G. L. Celardo, G. Cuniberti, A. Garcia-Etxarri, A. Dianat, I. Diez-Perez, Y. Guo, R. Gutierrez, C. Herrmann, J. Hihath, S. Kale, P. Kurian, Y.-C. Lai, T. Liu, A. Lopez, E. Medina, V. Mujica, R. Naaman, M. Noormandipour, J. L. Palma, et al., *ACS Nano* **2022**, *16*, 4989.
[23] R. Naaman, Y. Paltiel, D. H. Waldeck, *Nat. Rev. Chem.* **2019**, *3*, 250.
[24] S.-H. Yang, R. Naaman, Y. Paltiel, S. S. P. Parkin, *Nature Rev. Phys.* **2021**, *3*, 328.
[25] B. Göhler, V. Hamelbeck, T. Z. Markus, M. Kettner, G. F. Hanne, Z. Vager, R. Naaman, H. Zacharias, *Science* **2011**, *331*, 894.
[26] Z. Xie, T. Z. Markus, S. R. Cohen, Z. Vager, R. Gutierrez, R. Naaman, *Nano Lett.* **2011**, *11*, 4652.
[27] M. Kettner, B. Göhler, H. Zacharias, D. Mishra, V. Kiran, R. Naaman, C. Fontanesi, D. H. Waldeck, S. Sek, J. Pawlowski, J. Juhaniewicz, *J. Phys. Chem. C* **2015**, *119*, 14542.
[28] T. J. Zwang, S. Hürlimann, M. G. Hill, J. K. Barton, *J. Am. Chem. Soc.* **2016**, *138*, 15551.
[29] K. M. Alam, S. Pramanik, *Nanoscale* **2017**, *9*, 5155.
[30] A. K. Mondal, M. D. Preuss, M. L. Ślęczkowski, T. K. Das, G. Vantomme, E. W. Meijer, R. Naaman, *J. Am. Chem. Soc.* **2021**, *143*, 7189.
[31] V. Kiran, S. P. Mathew, S. R. Cohen, I. Hernández Delgado, J. Lacour, R. Naaman, *Adv. Mater.* **2016**, *28*, 1957.
[32] T. Liu, X. Wang, H. Wang, G. Shi, F. Gao, H. Feng, H. Deng, L. Hu, E. Lochner, P. Schlottmann, S. von Molnar, J. Zhao, P. Xiong, *ACS Nano* **2020**, *14*, 15983.
[33] H. Al-Bustami, S. Khaldi, O. Shoseyov, S. Yochelis, K. Killi, I. Berg, E. Gross, Y. Paltiel, R. Yerushalmi, *Nano Lett.* **2022**, *22*, 5022.
[34] Q. Qian, H. Ren, J. Zhou, Z. Wan, J. Zhou, X. Yan, J. Cai, P. Wang, B. Li, Z. Sofer, B. Li, X. Duan, X. Pan, Y. Huang, X. Duan, *Nature* **2022**, *606*, 902.
[35] Y. Adhikari, T. Liu, H. Wang, Z. Hua, H. Liu, E. Lochner, P. Schlottmann, B. Yan, J. Zhao, P. Xiong, *Nat. Commun.* **2023**, *14*, 5163.
[36] C. Kulkarni, A. K. Mondal, T. K. Das, G. Grinbom, F. Tassinari, M. F. J. Mabesoone, E. W. Meijer, R. Naaman, *Adv. Mater.* **2020**, *32*, 1904965.
[37] Y.-H. Kim, Y. Zhai, H. Lu, X. Pan, C. Xiao, E. Ashley Gaulding, S. P. Harvey, J. J. Berry, Z. Valy Vardeny, J. M. Luther, M. C. Beard, *Science* **2021**, *371*, 1129.
[38] J. Gersten, K. Kaasbjerg, A. Nitzan, *J. Chem. Phys.* **2013**, *139*, 114111.
[39] S. Alwan, Y. Dubi, *J. Am. Chem. Soc.* **2021**, *143*, 14235.
[40] L. Onsager, *Phys. Rev.* **1931**, *37*, 405.
[41] X. Yang, C. H. van der Wal, B. J. van Wees, *Phys. Rev. B* **2019**, *99*, 024418.
[42] X. Yang, C. H. van der Wal, B. J. van Wees, *Nano Lett.* **2020**, *20*, 6148.
[43] S. Dalum, P. Hedegård, **2019**, *Nano Lett. 19*, 5253.
[44] T. Liu, P. S. Weiss, *ACS Nano* **2023**, *17*, 19502.
[45] M. C. Hickey, S. N. Holmes, T. Meng, I. Farrer, G. A. C. Jones, D. A. Ritchie, M. Pepper, *Phys. Rev. B* **2007**, *75*, 193204.
[46] J.-I. Kim, T. Liu, K. Kountouriotis, J. Lu, X. Yu, Y. Adhikari, S. von Molnár, J. Zhao, P. Xiong, *Phys. Rev. Mater.* **2022**, *6*, 024603.
[47] Y. Fujita, M. Yamada, M. Tsukahara, T. Naito, S. Yamada, S. Oki, K. Sawano, K. Hamaya, *Phys. Rev. B* **2019**, *100*, 024431.
[48] T. N. H. Nguyen, L. Rasabathina, O. Hellwig, A. Sharma, G. Salvan, S. Yochelis, Y. Paltiel, L. T. Baczewski, C. Tegenkamp, *ACS Appl. Mater. Interfaces* **2022**, *14*, 38013.
[49] R. C. Tiberio, H. G. Craighead, M. Lercel, T. Lau, C. W. Sheen, D. L. Allara, *Appl. Phys. Lett.* **1993**, *62*, 476.
[50] S. F. Bent, *ACS Nano* **2007**, *1*, 10.
[51] C. L. McGuiness, D. Blasini, J. P. Masejewski, S. Uppili, O. M. Cabarcos, D. Smilgies, D. L. Allara, *ACS Nano* **2007**, *1*, 30.
[52] S. A. Claridge, W.-S. Liao, J. C. Thomas, Y. Zhao, H. H. Cao, S. Cheunkar, A. C. Serino, A. M. Andrews, P. S. Weiss, *Chem. Soc. Rev.* **2013**, *42*, 2725.
[53] O. Txoperena, F. Casanova, *J. Phys. D: Appl. Phys.* **2016**, *49*, 133001.
[54] M. Tran, H. Jaffrès, C. Deranlot, J.-M. George, A. Fert, A. Miard, A. Lemaître, *Phys. Rev. Lett.* **2009**, *102*, 036601.
[55] A. Dankert, R. S. Dulal, S. P. Dash, *Sci. Rep.* **2013**, *3*, 3196.
[56] T. Sasaki, T. Suzuki, Y. Ando, H. Koike, T. Oikawa, Y. Suzuki, M. Shiraishi, *Appl. Phys. Lett.* **2014**, *104*, 052404.
[57] J. Shiogai, M. Ciorga, M. Utz, D. Schuh, M. Kohda, D. Bougeard, T. Nojima, J. Nitta, D. Weiss, *Phys. Rev. B* **2014**, *89*, 081307.
[58] Y. Song, O. Chalaev, H. Dery, *Phys. Rev. Lett.* **2014**, *113*, 167201.
[59] V. Zarifis, T. G. Castner, *Phys. Rev. B* **1998**, *57*, 14600.
[60] Y. Song, H. Dery, *Phys. Rev. Lett.* **2014**, *113*, 047205.
[61] K. Hamaya, Y. Baba, G. Takemoto, K. Kasahara, S. Yamada, K. Sawano, M. Miyao, *J. Appl. Phys.* **2013**, *113*, 183713.
[62] M. K. Chan, Q. O. Hu, J. Zhang, T. Kondo, C. J. Palmstrøm, P. A. Crowell, *Phys. Rev. B* **2009**, *80*, 161206.
[63] F. Bloch, *Z. Phys.* **1930**, *61*, 206.
[64] P. Barate, S. H. Liang, T. T. Zhang, J. Frougier, B. Xu, P. Schieffer, M. Vidal, H. Jaffrès, B. Lépine, S. Tricot, F. Cadiz, T. Garandel, J. M. George, T. Amand, X. Devaux, M. Hehn, S. Mangin, B. Tao, X. F. Han, Z. G. Wang, X. Marie, Y. Lu, P. Renucci, *Phys. Rev. Appl.* **2017**, *8*, 054027.
[65] R. I. Dzhioev, K. v. Kavokin, V. L. Korenev, M. v. Lazarev, B. Y. Meltser, M. N. Stepanova, B. P. Zakharchenya, D. Gammon, D. S. Katzer, *Phys. Rev. B* **2002**, *66*, 245204.
[66] A. Fert, J.-M. George, H. Jaffres, R. Mattana, *IEEE Trans. Electron Devices* **2007**, *54*, 921.
[67] J. Fabian, A. Matos-Abiague, C. Ertler, P. Stano, I. Žutić, *Acta Phys. Slovaca* **2007**, *57*, 565.
[68] J. Fabian, S. Das Sarma, *J. Vac. Sci. Technol. B* **1999**, *17*, 1708.

[69] C. H. Shang, J. Nowak, R. Jansen, J. S. Moodera, *Phys. Rev. B* **1998**, *58*, R2917.
[70] H. J. Eckvahl, N. A. Tcyrulnikov, A. Chiesa, J. M. Bradley, R. M. Young, S. Carretta, M. D. Krzyaniak, M. R. Wasielewski, *Science* **2023**, *382*, 197.
[71] M. R. Safari, F. Matthes, C. M. Schneider, K.-H. Ernst, D. E. Bürgler, arXiv:2309.07588, **2023**.
[72] A. Chiesa, A. Privitera, E. Macaluso, M. Mannini, R. Bittl, R. Naaman, M. R. Wasielewski, R. Sessoli, S. Carretta, *Adv. Mater.* **2023**, *35*, 2300472.